# Journal Paper

## "Photovoltaic plant condition monitoring using thermal images analysis by convolutional neural network-based structure"

*- Renewable Energy-*

*2020*

Álvaro Huerta Herraiz
Ingenium Research Group, Universidad de Castilla-La Mancha
alvaro.huerta@uclm.es

Alberto Pliego Marugán
CUNEF-Ingenium, Colegio Universitario de Estudios Financieros de Madrid, Spain
alberto.pliego@cunef.edu

Fausto Pedro García Márquez
Ingenium Research Group, Universidad de Castilla-La Mancha
faustopedro.garcia@uclm.es

# Photovoltaic Plant Condition Monitoring using Thermal Images Analysis by Convolutional Neural Network-Based Structure

Álvaro Huerta Herraiz [1], Alberto Pliego Marugán [2], Fausto Pedro García Márquez [3]

[1,3] Ingenium Research Group, Universidad Castilla-La Mancha, 13071 Ciudad Real, Spain.

[alvaro.huerta; faustopedro.garcia]@uclm.es

[2] CUNEF-Ingenium, Colegio Universitario de Estudios Financieros de Madrid, Spain

alberto.pliego@cunef.edu

**Abstract.**

The size and the complexity of photovoltaic solar power plants are increasing, and it requires an advanced and robust condition monitoring systems for ensuring their reliability. This paper proposes a novel method for faults detection in photovoltaic panels employing a thermographic camera embedded in an unmanned aerial vehicle. The large amount of data generated by these systems must be processed and analyzed. This paper presents a novel approach to identify panels to detect hot spots, and to set their locations. Two novels region-based convolutional neural networks are unified to generate a robust detection structure. The main contribution is the combination of thermography and telemetry data to provide a response of the panel condition monitoring. The data are acquired and then automatically processed, allowing fault detection during the inspection. A detailed description of the methodology is presented, including the different stages to build the neural networks, i.e. the training process, the acquisition and processing of data and the outcomes generation. A thermographic inspection of a real photovoltaic solar plant is done to validate the proposed methodology. The accuracy, the efficiency and the performance of the approach under different real scenarios are evaluated statistically obtaining satisfactory results.

# 1. Introduction

Photovoltaic (PV) energy generation has been growing exponentially during the last decade. The global installed capacity has increased from 14 GWp in 2008 to more than 385 GWp in 2017 [1], i.e. a mean annual increase of 28% during the last ten years.

The installed capacity increased due to two main reasons: the extent of modern PV solar power plants is larger than before [2], covering areas with thousands of square meters, and; modern PV solar panels are more efficient, increasing the energy production [3,4]. For example, in 2008, the world largest PV solar plant was "Olmedilla PV Park" (Spain), with a capacity of 60 MW spread over 285 ha [5], whereas in 2017, it is "Shakti Sthala" (India), 2,000 MWp spread over 5,261 ha [6]. The difference of installed capacity between both plants is more than 1,940 MWp, being the extension of the newer plant more than 18 times greater.

Consequently, sophisticated systems require complex maintenance and operation (O&M) tasks [7,8], e.g. panel cleaning, lubrication, repairs and general inspections [9]. The O&M annually costs are estimated to be about 11.27 €/kWp in a ground installation [10], being the costs associated to planned inspection and monitoring around 1.47 €/kWp. Efficient methodologies and tools are needed to reduce the O&M costs and to improve the availability of the PV solar plants [11-13]. These approaches can facilitate both corrective and preventive maintenance [14-17].

This paper presents a method to process the data provided by an unmanned aerial vehicle (UAV) [18,19] fitted with a thermographic camera [20,21]. An 97% average increasing in inspection efficiency between aerial and to manual inspection time was found in reference [22] comparing, i.e. 1.07 €/kWp reduction.

The thermographic camera captures the infrared energy emitted by the objects [11]. The UAV allows thermal data to be acquired from better locations [23,24]. Hereinafter, the system composed of the UAV and the IR camera will be named as IR-UAV system. This system provides two different types of data: the IR images captured by a thermographic camera are collected in a matrix that assigns a temperature value to each pixel; telemetry data are provided continuously by the UAV, e.g. Global Positioning System (GPS), coordinates, altitude, orientation, etc. The system can record large amount of data in few minutes, e.g. around 2 Gigabytes in ten minutes. This paper proposes an advanced method to analyse automatically these data. Figure 1 shows a basic scheme of the complete data acquisition system.
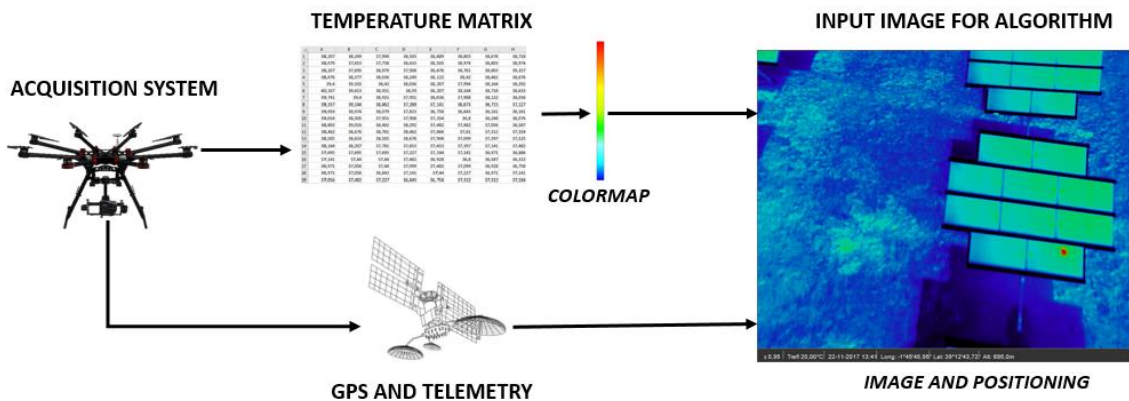


Figure 1. Data acquisition and image composition: An UAV equipped with thermographic camera obtains images from solar modules; A temperature matrix is generated, and a processing algorithm is used to detect relative hot spots; The telemetry is added for hot spots localization.

The thermal images can be employed to detect relative hot regions, associated to some failures, e.g. damaged cells, short circuits and fire hazards, etc. [25]. The telemetry data can be used to locate these hot spots. An artificial neural network (ANN) based methodology is developed to recognize panels and detect faults. The results of the image processing together with the GPS position are presented in a final report. This information facilitates the maintenance management, since the hot spots and failures in the PV solar power plant can be mapped.

The main contributions of this paper are:

- The paper proposes a combination of thermography, GPS positioning and convolutional neural networks (CNN) for fault detection in PV solar panels. Several authors have employed some of these techniques but not all techniques together. For example, Acciani *et al.* proposed a generic analysis of PVs using thermography [26,27], concluding that dirt can be identified as dark regions in thermal images. J. Muñoz *et al.* studied the risk of hot spots, that can cause irreversible damage in modules, appearing in PV solar cells and also in resistive solder bonds [28]. M. Aghaei *et al.* studied the applications of UAVs in PV solar plants maintenance [29]. They performed two experiments: the UAV flew for 5 minutes and monitored some panels in a roof; the second flight was in a PV solar plant. This inspection method had some limitations due to is was a visual method and image processing was not included. However, they confirm that UAVs result an efficient, cheap and reliable inspection tool. Kim *et al.* developed a method for detecting failures automatically in PV modules. They employed an UAV equipped with thermographic camera [30]. They obtained the panel area with their own algorithm and created an intensity histogram for each panel [31]. The automatic detection method was a pattern recognition based on histograms and statistical characteristics between good and defective panels. Unlike the method presented in this paper, they did not employ telemetry or GPS data to determine the location of the faults.
- The method allows to detect and located faults automatically. Literature shows similar techniques to locate faults. For example, Tsanakas *et al.* elaborated an advanced inspection system based in UAVs and thermal images [32]. They developed a technique with true orthophoto mapping, based on aerial triangulation and also GPS techniques. They concluded that GPS was more effective than aerial triangulation, especially in large areas. However, this method is not an automatic detection process.
- This work employs artificial intelligence to detect faults in PV panels. Similar works can be found in the literature [33], however, they do not combine the region-based convolutional neural networks (R-CNN) and telemetry data. Thermography in PV solar panels has been developed on laboratories to study or identify hot spots, or cracked silicon wafers [28,34]. ANN based methods, in particular R-CNN, are often used to the object detection and classification in images [35], even real-time object detection [36]. Some authors use pretrained networks suitable to current object detection, e.g. AlexNet or GoogleNet [37]. However, they cannot detect relative hot regions since they are not a common object. This tool is also employed in the automotive sector to detect signals [38], vehicles or pedestrian [39]; in medicine to detect tumours [40] or face detection [41]; and in manufacturing industry for process automation [42]. Regarding the positioning system, a similar technique can be found in reference [43], where the positioning of the UAV is improved by integrating a GPS/INS/Vision sensors (INS: inertial navigation systems). However, this positioning system is not integrated in a R-CNN.
- The method is validated and applied in real PV solar plants. Most of the works about thermography inspection of PV solar panels focus on the analysis of individual panels. In those works, different methods were applied to demonstrate the capabilities of thermography, for example, studying the efficiency of the panel [26], detecting relative hot regions in panels [44] or identifying general faults in PV modules [45]. However, the proposed method is employed in a real PV solar plant, where many panels can be analyzed together.

Therefore, the main contribution of this paper with respect to the literature is the development of an intelligent algorithm that detects and allocates automatically relative hot areas of solar panels. The algorithm is tested in a real PV solar farm.

The paper is structured as follows: Section 2 describes the IR-UAV based data acquisition system. Section 3 explains the CNN and the R-CNN structure. Section 4 shows the method together with the training, data acquisition and processing stages. Section 5 validates the method in a real PV solar plant by comparing the outcomes of the method with the real dataset.

## 2. Infrared cameras embedded in UAVs and PV solar panels

Thermography is a non-destructive evaluation (NDE) technique [20,46-48]. Therefore, it allows to inspect components and materials without modifying their structural or physical integrity. It is based on the infrared radiation (IR) that objects emit [49].

Thermographic inspections can provide the operating status of the PV panels using a thermographic pattern identification of relative hot areas. Further details about these patterns can be found in references [50] and [51]. This information can be used for detecting faults or abnormal performances.

There are two types of IR thermography techniques: *active techniques*, which employ an external source that adds extra energy to the object, generating an internal heat flow and increasing the temperature, and; *passive techniques*, that measure the radiation from the matter without using any external heat source.

The approach proposed in this paper employs radiation data collected by passive thermographic methods, i.e. the acquisition system only needs a camera without any power heat systems. The suitability IR-UAV system depends on the following aspects:

**UAV specifications:** the UAV must be safe and stable. The most determining parameters are:

- *Power* is the capacity in watts of the UAV. The power will determine variables such as the total admissible weight, the battery consumption and the power of DC motors.
- *Autonomy* is the estimated flight time of the aircraft. It depends of, for example, the weight or the wind speed.
- *Weight* depends on the type of UAV and the on-board equipment, e.g. camera, sensor or video transmitters.
- *Gimbal* is the device that controls the movement of the camera. It usually has pan, tilt and roll movements. It is essential for controlling the camera.

**IR camera features:** it must be able to take thermal and visual images and to provide telemetry and GPS data. The most important parameters of the camera are [52]:

- *Resolution* corresponds to the density of pixels of the images. High-resolution cameras allow usually smaller areas to be scanned without losing the quality of the image. The available information depends on the resolution of the detector.
- *Focal length* is de distance between the convergence point and the imaging sensor. It determines the angle of view and, therefore, the area recorded [53].
- *Temperature range* is the difference between the maximum and the minimum temperatures that can be recorded by the IR camera.

- *Emissivity* is related to the energy that matter radiates to the exterior. The emissivity is adjusted in the camera depending on the object to analyse. Emissivity values could vary with the surface condition of the measured object, and also with temperature variation and wavelength. A variation in emissivity values will cause an alteration in the measure [51].

The hour of the day and the date are key variables for the experiments. The acquisition system has been designed considering that each PV solar plant has a different shape or design, either related to the configuration of panels or the conditions of the terrain in that are installed.

**Configuration of the plant and the panels:** Figure 2 shows some configurations for PV solar trackers and panels. In case of ground installations, it is common to place the modules in a row as shown in Figure 2(d). If the panels are installed in PV solar trackers, they can be configured according to different patterns, see Figure 2(a, b, c).



|        (a)        |        (b)        |        (c)        |        (d)        |
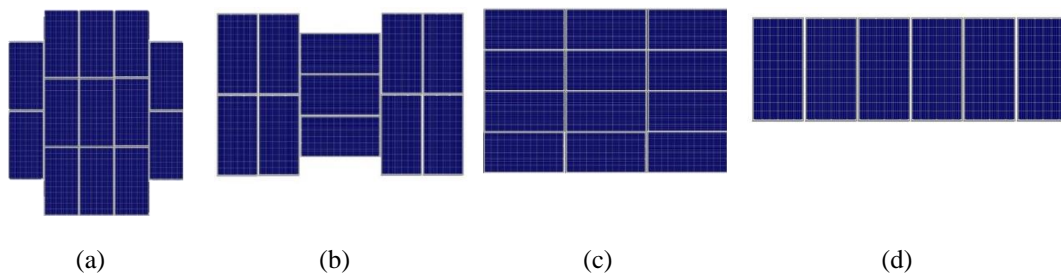
Figure 2. Different panel configuration: PV solar tracking with one or two axes (a), (b) and (c); ground installation (d).

**Orientation of the UAV and the IR camera**. The images should be taken in perpendicular to the PV panel, where panels have square or rectangular contours in the image. The time and the date of the flight require to be considered to avoid reflections because they could cause confusions with relative hot region or other faults [54]. The altitude of the UAV determines the number of panels inspected, where duplicated information would appear in several frames.

**Reflections** are a common problem in thermography inspections. It affects to the image resolution and the precision. Accurate measurements only will be possible when the image signal presents a high noise equivalent temperature-difference (NETD) [54]. In case of reflections, the approach could detect brightness instead of relative hot regions.

**Duplication of data**. A panel or a set of panels may appear several times in different frames since several images are inputted into the approach. An algorithm to manage these duplications is needed before the results.

An adequate combination of these factors allows high-quality thermographic inspections to be carried out.

## 3. Convolutional neural networks

ANN is an advanced and robust method based on biological neural networks. They are usually composed of the following elements:

- *Neurons* are the processing units. There are three types of neurons grouped in layers: input neurons, output neurons and hidden neurons. The input layer receives the data, the hidden layers link the inputs and the outputs, and the output layer provides the outcomes of the ANN.

- *Activation function* defines the output of each neuron according to its inputs. The activation value can be continuous or discrete.
- *Connection between neurons* is a certain value adjusted during the training stage and reflects the knowledge acquired by the net.

ANNs learn to interpret the data by a training process. Then, the data can be classified according to the learned patterns [33]. However, the ANNs require a large computational cost for processing images. These images need a high number of connections between neurons and require large processing periods. This problem can be addressed by using CNNs.

CNNs belong to the family of Deep Neural Networks, whose main characteristic is the use of multiple convolution layers [55]. Their structures are different from conventional ANNs such as perceptron [56]. CNNs have some layers only connected to a subset of neurons in the next layer, reaching a high processing speed. Figure 3 shows a comparison between ANN (left) and CNN (right).
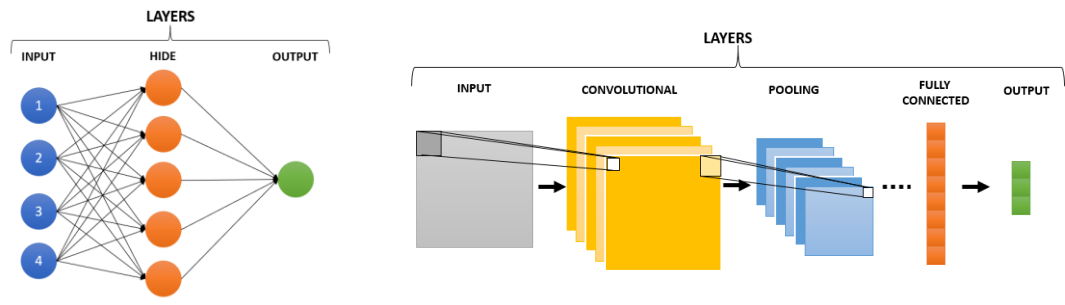


Figure 3. Comparison of ANNs and CNNs [57]. All the layers are fully connected to the neighbor layers in a typical ANN. The CNN include convolutional and pooling processes.

CNNs usually consist of two stages: feature extraction and classification [58]. The first stage is composed of alternative layers of convolutional neurons and sampling reduction neurons. Distinctive features of the image, such as edges or textures, are extracted in this stage. The objective is to classify different regions by fully connected layers.

Several authors have demonstrated the effectivity of a type of CNN for object detection and semantic segmentation (SDS), called R-CNNs. Hariharan *et al.* trained a two column R-CNN for traditional bounding box detection and for semantic segmentation [59]. Gkioxari *et al.* trained an R-CNN to detect people and to recognise their positions and actions. They joined several networks obtaining similar results to individual networks, but N-times faster [60]. Due to their efficiency for generic object detection, R-CNNs are proposed in this paper for PV solar panel and relative hot region detection.

The structures of these networks are based on the following layers:

*Convolutional layers* are sets of filters capable of learning by a training stage [61]. These filters are convoluted along the input image. The number of neurons ($N$) is given by equation (1):

$$N = \frac{(W-F+2P)}{S} + 1,$$
(1)

where:

- $W$ is the input volume.
- $F$ is the spatial extent.
- $S$ is the stride of the convolution.
- $P$ is the zero padding on the border.

6

A zero-padding is used to ensure that the input and the output have the same size. A zero-padding is a process that pad the input volume with zeros around the border. To control the output volume, the zero-padding is used and the stride ($S$) is set at 1. Then, the zero padding ($P$) is defined by equation (2):

$$P = \frac{(F-1)}{2}.$$ (2)

An input size of $W_1 \, x \, H_1 \, x \, D_1$ will generate an output size of $W_2 \, x \, H_2 \, x \, D_2$. These parameters are defined by equation (3):

$$W_2 = \frac{(W_1 - F + 2P)}{S} + 1; \quad H_2 = \frac{(H_1 - F + 2P)}{S} + 1; \quad D_2 = K;$$ (3)

where $K$ is the number of filters of the convolutional layer.

*Pooling layer:* is commonly inserted between different convolution layers. This layer is used for a progressive reduction of the spatial size of the representation. The number of parameters and the computational cost will be reduced. The pooling layer has a size of $W_2 \, x \, H_2 \, x \, D_2$. The output will be a volume of dimensions $W_3 \, x \, H_3 \, x \, D_3$, where:

$$W_3 = \frac{(W_2 - F)}{S} + 1; \quad H_3 = \frac{(H_2 - F)}{S} + 1; \quad D_3 = D_2;$$ (4)

*Rectified Linear Unit (ReLU) layer:* it is a complementary step to the convolution operation. Some authors consider that it is a part of the convolutional layer. In this paper, it is considered as a separated layer because of the programming language employed [62]. This layer employs an activation function [63,64]. This function can be defined by equation (5).

$$f(x) = \begin{cases} x, & x \geq 0 \\ 0, & x < 0 \end{cases}$$ (5)

*Fully-connected layer:* the neurons are connected with all the activation functions of the previous layer. The input is pondered by a weight matrix and a bias vector is added. The objective of this layer is to classify the input image through the features obtained previously. This layer is usually followed by a SoftMax Layer.

*SoftMax layer [65]:* It is used as a classifier. The probabilities of each class are calculated with a confidence level. The SoftMax model is often considered as a part of the fully connected layer. The advantage of using SoftMax is that the sum of the output vector is 1 and there are not negative values, therefore, each component can be considered the probability of each class. The same vector could be also obtained by employing the Sigmoid function when the number of output classes is 2. The SoftMax model is a generalization of the sigmoid function for multiclass prediction. The use of SoftMax would allow to the ANN to be improved in case that more classes, such as specific faults, need to be predicted. Each node of this layer receives the information from all the nodes of the previous layer. The total input of the SoftMax layer ($a_i$) is given by equation (6).

$$a_i = \sum_k h_k M_{ki}$$ (6)

being:

- $h$ is the activation function of the previous layer nodes.
- $M$ is the weight connecting the previous layer to the SoftMax layer.

For $X$ number of classes, this layer contains a total of $X$ nodes denoted as $p_i$ [66], where $p_i$ is a discrete probability function, so that $\sum_i^X p_i = 1$. The probability value assigned to each class is:

1    $$p_i = \frac{exp(a_i)}{\sum_j^X exp(a_j)} \qquad , \text{where } i = 1, \dots, X \tag{7}$$

2    Finally, since $p_i$ is dependent on $a_i$, then the predicted class $\hat{i}$ is given by:

3    $$\hat{i} = arg \max_{\hat{i}} (p_i) \quad \text{or} \quad \hat{i} = arg \max_{\hat{i}} (a_i) \tag{8}$$

4    Figure 4 shows the operations carried out by each different layer of the R-CNN.
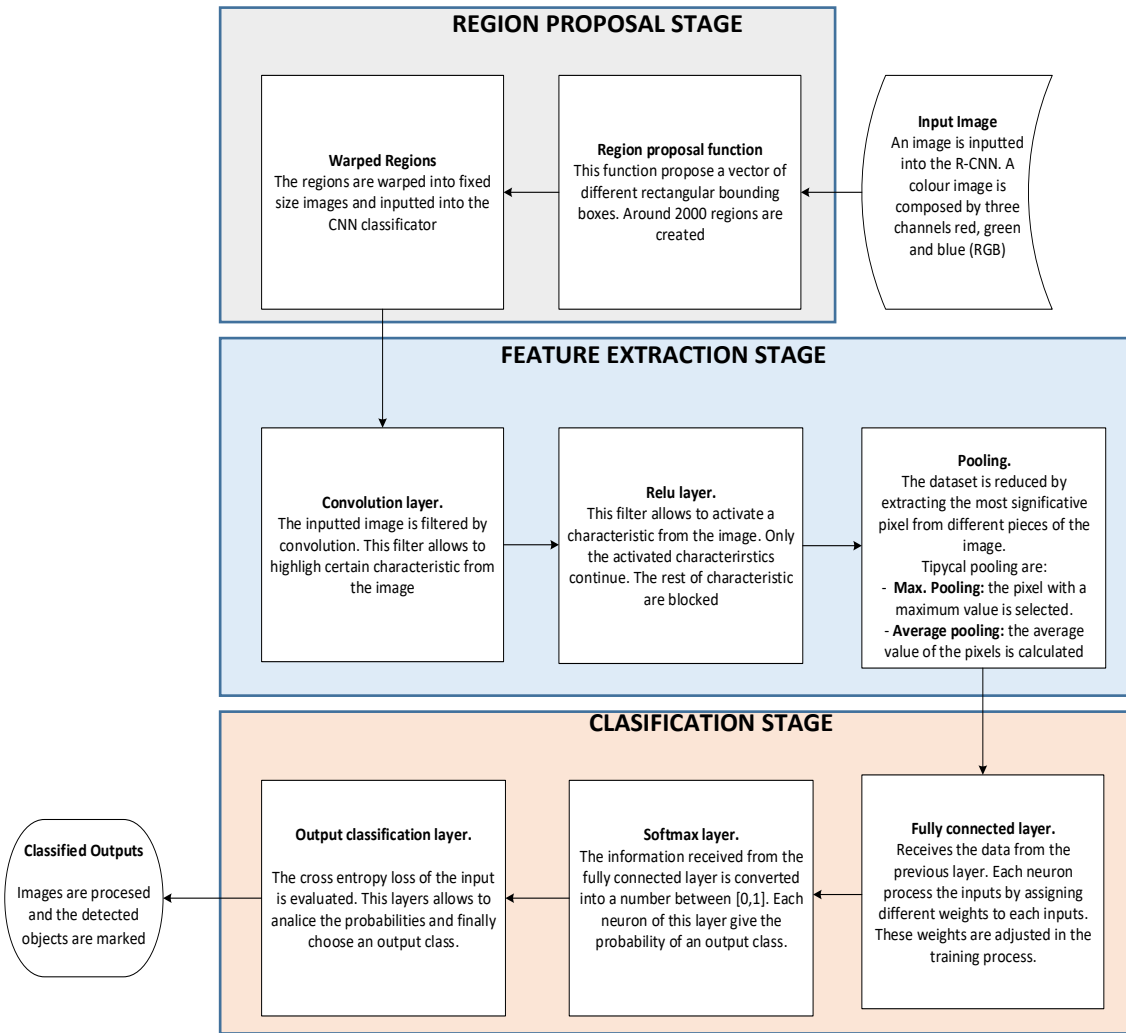
5


6    Figure 4. Scheme of R-CNN functioning, being the region proposal step is a specific stage of the R-
7    CNN.

8    The class prediction is the basis for the detection system. Figure 5 shows the scheme of the
9    detection system proposed in this paper [36]. An image is selected and the regions of interest
10   (ROI) are marked (Figure 5.2). This step is accurately developed by experts using specific
11   labelling software, e.g. see reference [67], obtaining a database with the images ant the location
12   of panels and relative hot regions in the image. Then, the images are computed by the R-CNN
13   (Figure 5.3) that provides a final classification (Figure 5.4)).
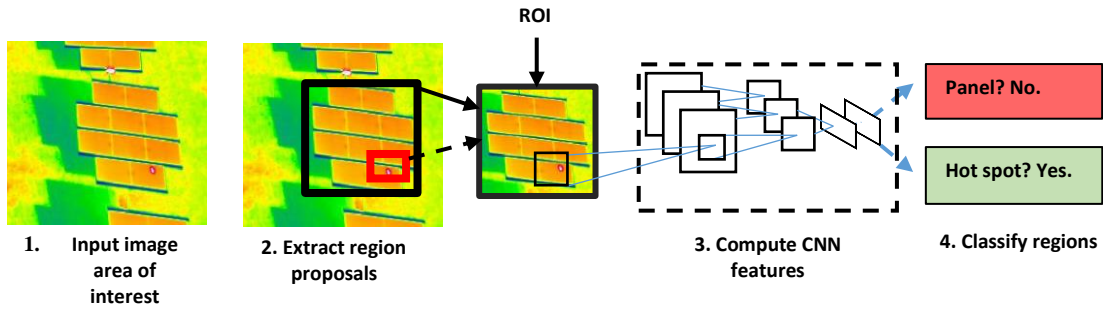
Figure 5. Scheme of object detection system based on region-based convolutional neural networks: An image is inputted (1); Several regions are proposed and evaluated (2); These regions are inputted in the CNN classifier (3); A final classification is provided (4).

The success of the R-CNN depends on several variables, e.g. the applicability of the input database, the volume and the representativity.

## 4. Novel Approach

This section describes novel methodology for detecting and locating relative hot regions. The algorithm is divided into three main stages: a R-CNN based structure is created and trained by using real image of solar panels; the R-CNN is employed for processing new data from the IR-UAV system, and; the results are summarized in a report, considering both telemetric and thermal information. Figure 6 shows the flowchart of the method.
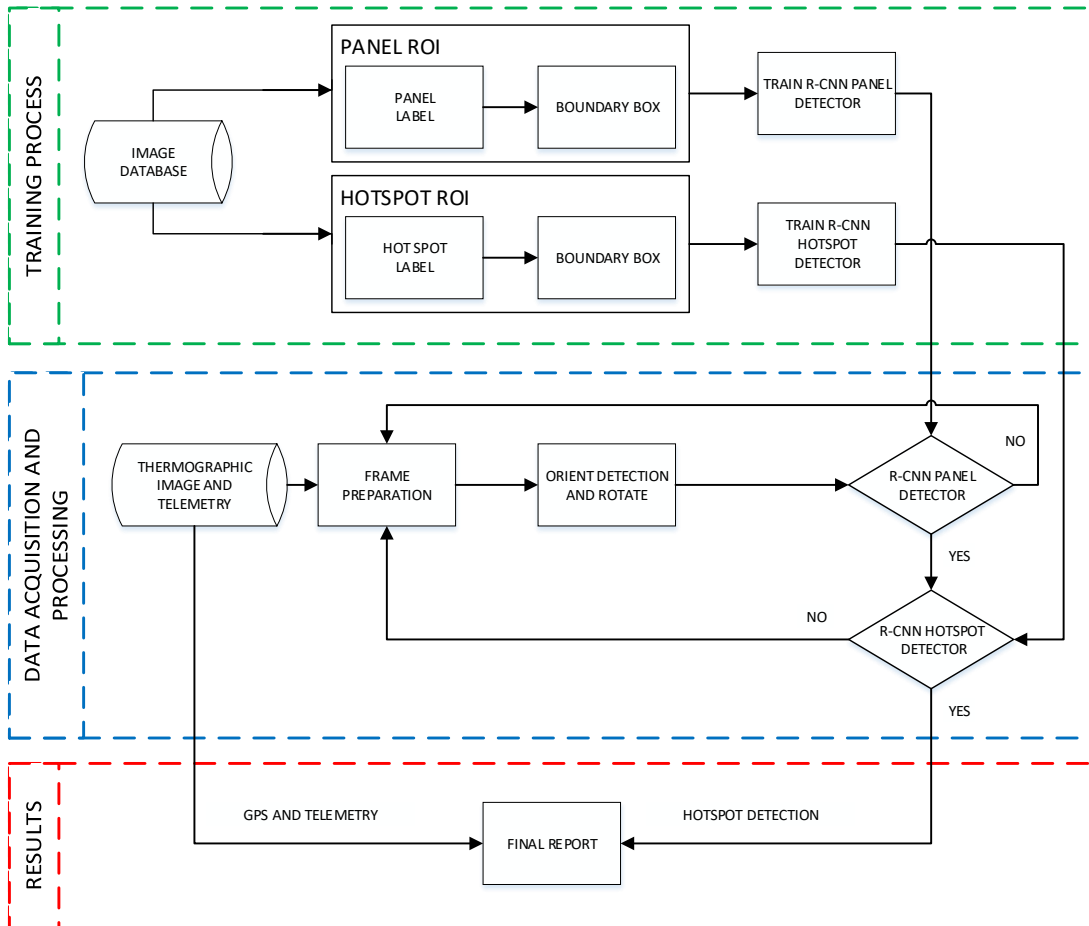


Figure 6. Flowchart of the proposed algorithm.

*a) Training process*

2   The first step is the generation of a database using images of a PV solar power plant. The training
3   image set employed is based on 800 images, including 320 hotspots.  Different types of panels,
4   shapes, sizes and orientations must be included. The training process has been done in this paper
5   by selecting the individual frames and labeling the ROIs in them. Each ROI is a rectangular
6   window defined by four points $(X, Y, H, W)$, i.e. the top-left corner $(X, Y)$, the height $(H)$ and
7   weight $(W)$ [68]. Two types of ROIs will be considered in this paper: A Panel Set ROIs and
8   Relative hot regions ROIs. The creation of the ROIs requires the definition of the labeling and the
9   boundary box.

10   The labeling stage is to determine the type of ROI. The boundary box will determine the area of
11   the image that the ROI is covering. Figure 7 shows an example of the ROIs definition during the
12   R-CNN training process.
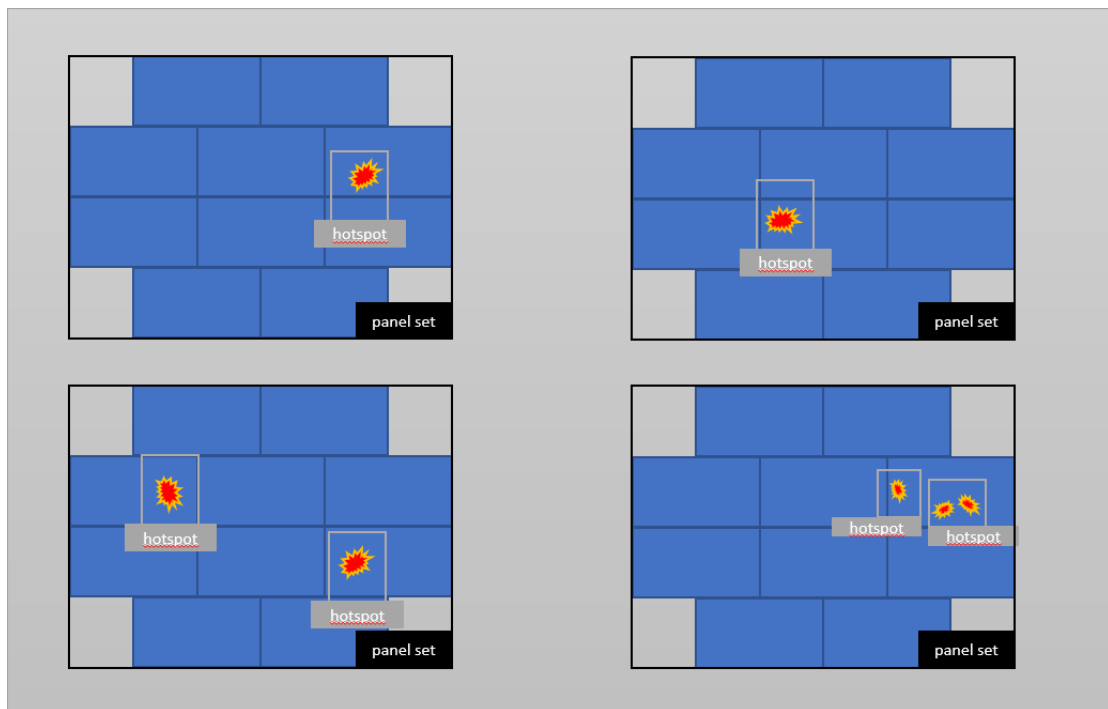
13



14        Figure 7. ROIs definition during the R-CNN training process. The labels are employed in the training
15                            process.

16   The training images are ready to be inputted in the R-CNN when the ROIs have been defined. It
17   is necessary to fix the training options before starting the training stage, including:

18       - *Initials weights and biases:* these values are employed in the design of the Convolutional
19          layer and the Fully Connected Layer. By default, they are a Gaussian distribution with a
20          mean of 0 and a standard deviation of 0.01. The weights and biases are updated with the
21          Stochastic Gradient Descent (SGD) algorithm  in order to minimize the loss function [69].
22       - *Initial learn rate:* used for initial training. An initial learn rate of $10^{-6}$ has been used. A
23          low learn rate leads a slow training process, but a high learn rate could provide inaccurate
24          results.
25       - *Learn rate schedule*: it allows the learn rate to be modified during the training stage. This
26          learn rate is proportional to the called "*Learn rate drop factor*". No learn rate has been
27          required in this training.
28       - *Learn rate drop factor:* used in case that the learn rate schedule is active.

1      -    *Learn rate drop period:* is applied to the learn rate schedule and defines the period of
2             epochs to apply previous factor.
3      -    *Max epochs*: 15 epochs have been found as the optimal. The number of epochs determines
4             the number of times that the training algorithm is applied to the whole training dataset.
5             The time required by the training process depends on this parameter.
6      -    *Mini batch size:* adjusts the batch size. With a batch size of 16, optimal results have been
7             obtained. This batch is a subset of the training image set. The SGD algorithm uses the
8             parameter mini batch size as a parameter to evaluate the gradient at each iteration. A
9             gradient clipping stabilizes the higher training learning rates in case of exponential
10            increasing of the gradient.

11 The selection of both the batch size and the max epochs has been done by iterating the
12 algorithm with different values. Figure 8 shows that a higher max epochs number reduces the
13 error, however the computational time increase. Similar results can be found in reference [70].
14 It can be observed that the error become stable from 15 epoch.
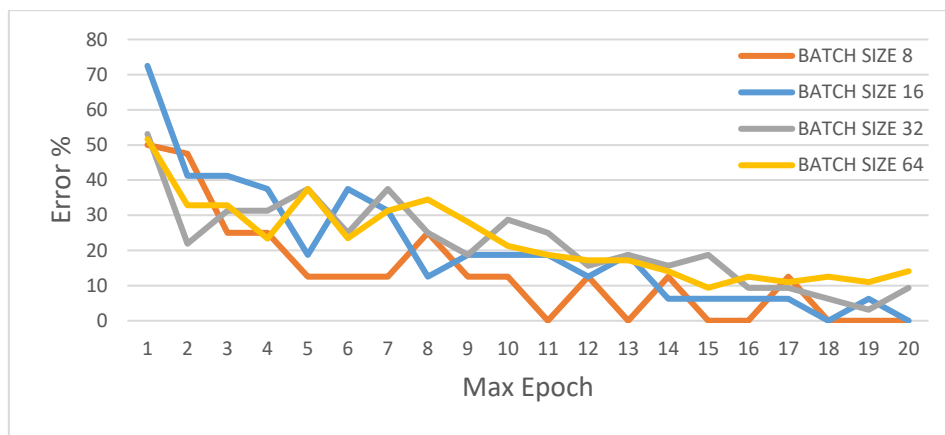


15

16 Figure 8. Max. Epoch vs Error during the R-CNN validation process for different batch sizes. The
17 error decreases when the maximum number of epochs is higher.

18

19 Figure 9 shows the computational time required by the algorithm to complete the image
20 processing for different batch sizes and 15 max. epochs. In this case study, the computational cost
21 decreases for higher batch sizes. Therefore, a batch size of 16 is selected instead of 8. These
22 parameter selection leads to reduce the computational cost without an excessive loss of accuracy.
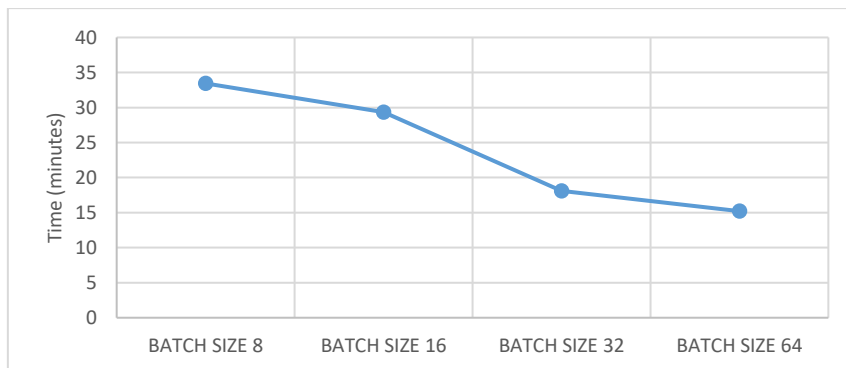


23

24 Figure 9. Batch size vs. running time. In this case study, a reduction of running time is observed
25 when the minimal batch size increases.

26

1  Table I shows a resume of the training options and structural parameters considered for the
2  proposed R-CNN.

3                                   Table I. Parameters of R-CNN

| Parameters | Values |
| --- | --- |
| Initial learning rate | $10^{-6}$ |
| First convolutional layer filter size | 5x5 |
| No. of filters in the first convolutional | 32 |
| Second convolutional layer kernel size | 5x5 |
| No. of filters in the second convolutional | 32 |
| Third convolutional layer filter size | 5x5 |
| No. of filters in the third convolutional | 64 |
| Max. pooling layer kernel size | 3 |
| No. of neurons in the fully connected layer | 2 |
| No. of epoch | 15 |
| Min batch size | 16 |

4

5  The convolutional layers are created after the training options. The method employs a R-CNN
6  with 15 different layers including input, convolution, ReLU, pooling and output layers. Figure 10
7  shows the architecture of the developed R-CNN, that is based on the architectures given in
8  references [71], [72] and [73].

9
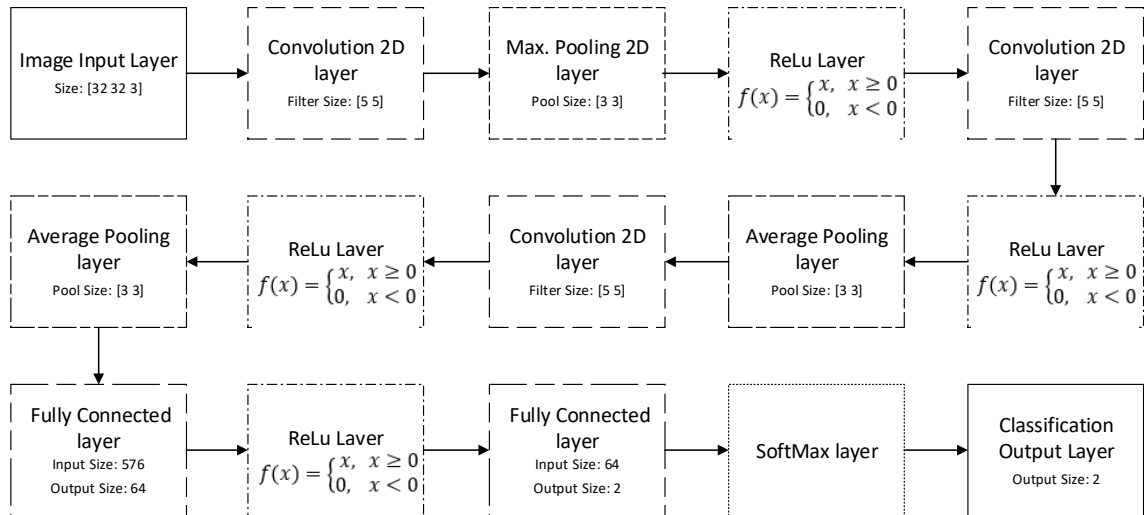


11                          Figure 10. CNN architecture based on layers.

12  The training process is a complex task that could take several hours, even days, depending on the
13  number of images, boundary boxes and labels, and on the GPU or CPU characteristics. The
14  training algorithm is according to reference [74]: a Region Proposal Network is pre-trained to
15  generate a set of proposals; a new detection network is trained by using the proposals generated;
16  the detector network is employed to initialize the RPN training, and; the convolutional layers
17  shared by both networks are fixed and the fully connected layers are tuned. Consequently, the
18  networks share the convolutional layers to create a unified structure. Once the R-CNN has been
19  trained, it is ready to receive real images from the data acquisition system.

20

*b) Data acquisition and processing*

The telemetry data provided by the IR-UAV system contain the altitude, orientation, GPS position, camera angle and vision angle. The data will be added to the final report if a relative hot region is detected.

The R-CNN provides better results if the edges of the PV solar panels are perpendicular to the edges of the images because of the ROIs are square. Therefore, it is convenient to orientate the image to improve the detection task. For this purpose, a code has been developed using an edge detection algorithm. It is based on derivative approximation method [75], developed through the Sobel model. The bounds are considered to be the points where the gradient is maximum. The edges of the images are detected using this information, and the algorithm is able to find the predominant directions to rotate the image. Figure 11 shows, from left to right, the different steps of the image rotation process.
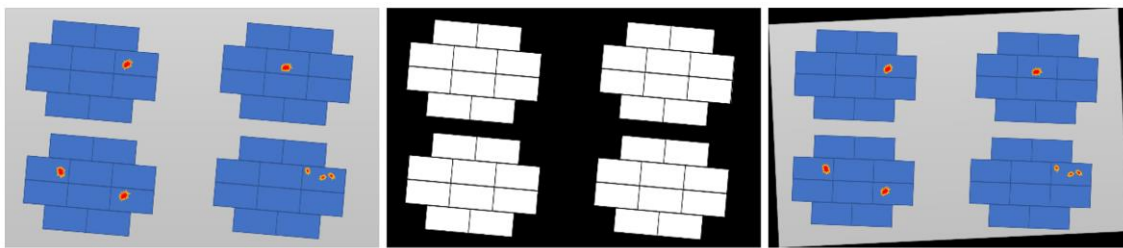


Figure 11. Input image (Left); Edge detection (Middle): This image shows an intermediate step in which the contours of the solar modules are detected; Rotated image (*Right):* the contours of the panels are parallel to the edge of the image.

The detection algorithm is developed to assign a score to each boundary box and a confidence scores to each detected object. Only those results with a high confidence (more than 0.9) will be considered in this paper. Figure 12(a) shows an example of boundary boxes detection. The approach will search relative hot region only in the PV ROIs identified. Relative hot regions detected outside boundary boxes will be discarded since they can be generated by reflections, stones, or other external elements. The image is analysed with the R-CNN relative hot region detector. Figure 12(b) shows the outcome.



(a)                                                                (b)
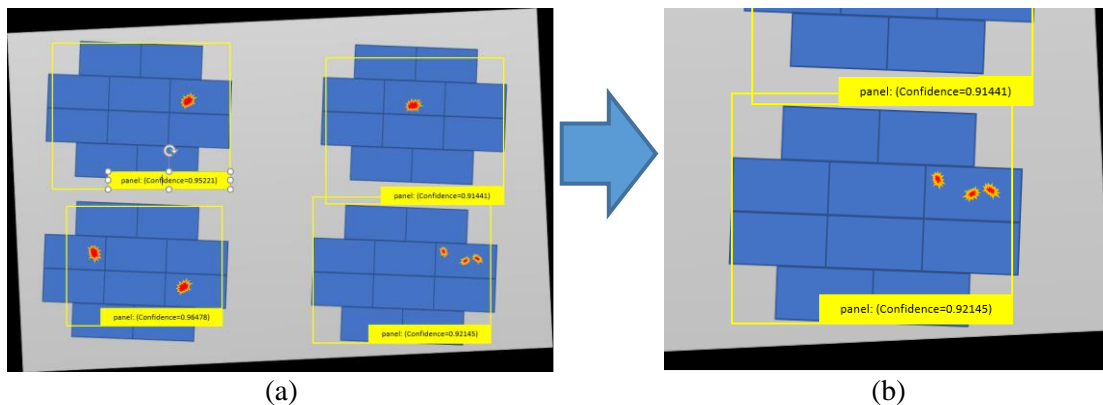
Figure 12. Output of pretrained R-CNN (a) and result of relative hot region detection (b).

The final stage of the approach is to associate the telemetry data and the outcomes in case that any relative hot region has been detected.

1 *c) Relative hot region localization*

2 The approach outcomes and the telemetry data are joined to generate a final report. The GPS
3 position is combined with the altitude, the UAV orientation, the camera angle and the focus angle.
4 Figure 13 shows a basic scheme the area of interest together with the variables. The area of interest
5 is the real portion of ground taken by IR camera in a specific frame. On the other side, the ROI is
6 the region inside the area of interest that will be analyzed.
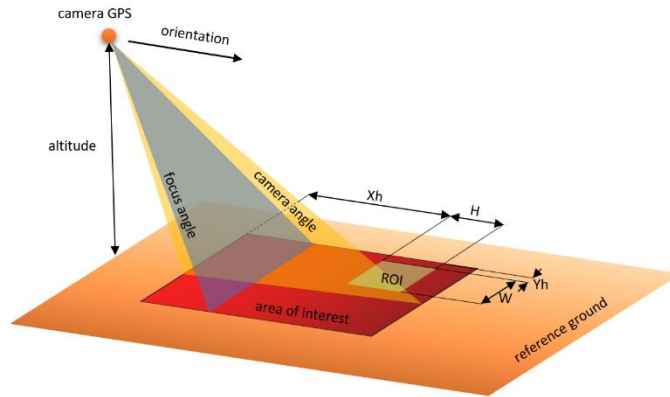
7



8 Figure 13. Area of interest (red square): This area is considered as the total area captured in a frame.
9 ROI (yellow square): contains the area that will be analysed. Camera and focus angles are shown by
10 yellow and grey triangles respectively.

11 The following parameters are considered for calculating the position of the damaged PV module
12 (see Figure 14):

13 - Altitude (z), Zenithal angle ($\theta_{ZD}$) and Azimuthal angle ($\Psi_{ZD}$), provided by the telemetry
14    system.
15 - The field of view angle ($\Upsilon$) of the thermographic camera.
16 - Location of the relative hot region within the IR image ($X_h, Y_h$).
17 - Coordinates of the drone ($x_D, y_D$), provided by the GPS.

18 This information is processed through trigonometric. The area of interest coordinates
19 ($x_{f1}, x_{f2}, y_{f1}, y_{f2}$) and the coordinates of the damaged panel ($x_P, y_P$) are obtained. Figure 14
20 shows two perspectives to visualize the information provided by the GPS and the telemetry
21 system together with the coordinates above mentioned.
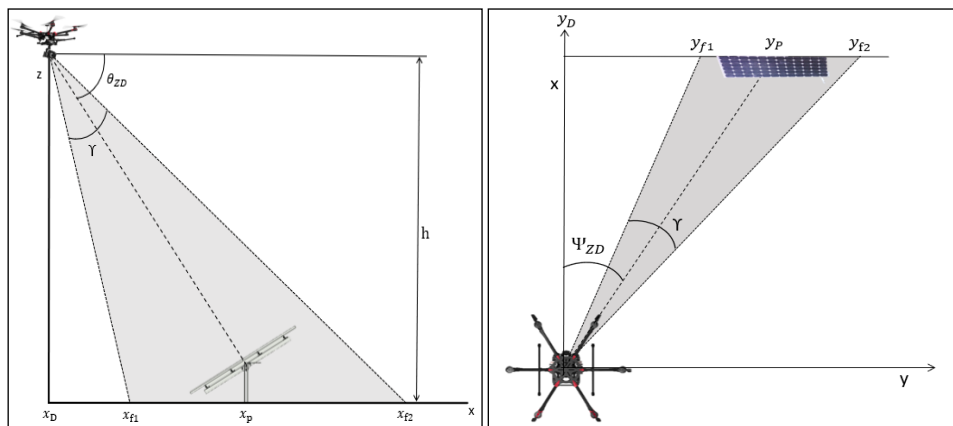
22



23 Figure 14. Different perspective of the location of panels with relative hot regions, and distances
24 and angles employed for their localizations.

The following expressions are employed to obtain the coordinates in the ground according to Figure 14:

$$y_{f1} = h \cdot tan(90 - \theta_{ZD} - 0.5\,\Upsilon)$$

$$y_{f2} = h \cdot tan(\theta_{ZD} - 0.5\,\Upsilon)$$

$$x_{f1} = y_{f1} \cdot tan(\Psi_{ZD} - 0.5\,\Upsilon)$$

$$x_{f2} = y_{f2} \cdot tan(\Psi_{ZD} - 90 - 0.5\,\Upsilon)$$

Therefore, the relative hot region location is given by:

$$x_P = x_{f1} + X_h$$

$$y_P = y_{f1} + Y_h$$

$x_P$ and $y_P$ are set into GPS coordinates to show to the operators the allocation of the faults. Nowadays, any fault is usually manually checked by operators before starting any task. The GPS and the telemetry systems are subject to errors that depend of the system.

### d) *Results*

The final report presents a table with two columns. The rows correspond to each fault detected. The first column contains the GPS coordinates of the area of interest. The second column defines the position of ROI. The results vary if the telemetry data are not accurate enough [76]. Figure 15 shows an example of a final report. The four points $(X_h, Y_h, H, W)$ define in which position of the image the relative hot region are detected, $(X_h, Y_h)$ are the start point of the relative hot region, and $(H, W)$ are the size in pixels of the boundary box. It is combined with the GPS telemetry specified in each frame to determine the final position.

| GPS Latitude/Longitude | $X_h/Y_h/H/W$ |
|---|---|
| 39.2127/-1.7629 | 492/231/90/33 |
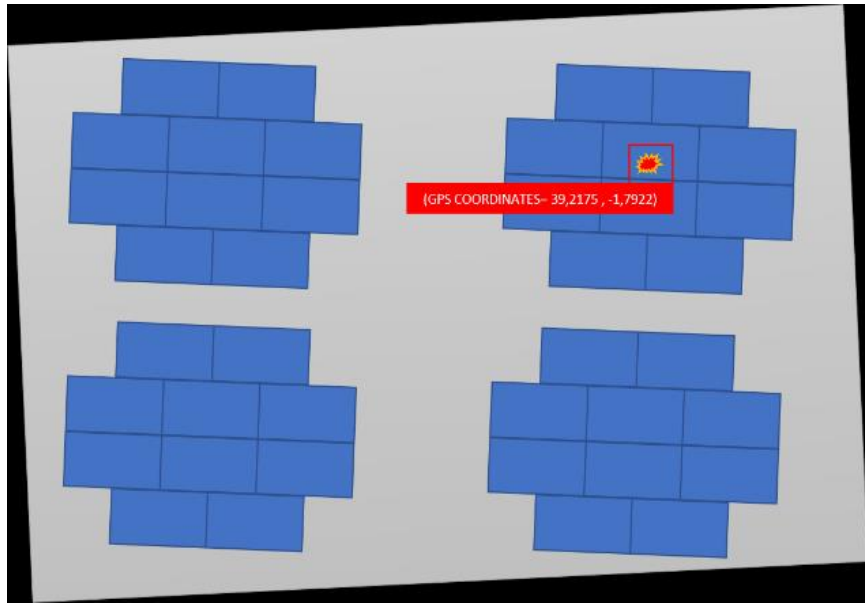
Figure 15. Relative hot region and GPS location. Combination of IR image and telemetry. The final report shows a table with the GPS coordinates of hot spots.

## 5. Case study and validation of the method

The approach has been implemented and used for inspecting a real PV solar plant of 100 kWp. Figure 16 shows the main image processing and hotspot detection steps for one example thermal image of the solar park. Figure 16(a) contains a thermal image of a PV solar plant collected by the IR-UAV system. It has 640x534 pixels and a 32-bit color depth. The telemetry data, together with the emissivity and the acquisition date, are included at the bottom of each image. Figure 16(b) shows the edge detection process used for rotating the image. Figure 16(c) shows the result of the rotation process. Figure 16(d) presents the outcome of the R-CNN panels detector. Figure 16(e) shows the outcome of the R-CNN relative hot region detector. Finally, Figure 16(f) contains the relative hot regions labeled with the specific estimated location.



(a)　　　　　　　　　　(b)　　　　　　　　　　(c)
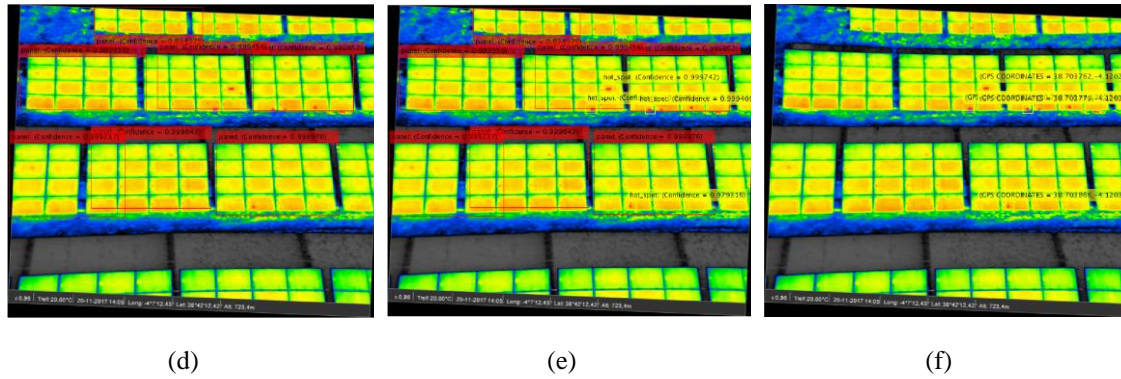
| (d) | (e) | (f) |

Figure 16. Real case study: (a) Thermal image (b) Contour detection. (c) Image rotated. (d) Panel detection. (e) Relative hot region detection. (f) Location of relative hotter regions.

The R-CNN works with square ROIs. The ROI presents an error that depends of the training images, the orientation of the panels, the temperature of the edges, etc. They are trapezoidal because of the perspective of the images deforms panels. Therefore, the contour of the panels cannot be exactly marked by the panel ROIs. The relative hot area is always located inside a panel ROI, therefore, it is not considered an external hot element as anomaly in the panels.

The locations of the relative hot regions are obtained by the telemetry data given by the camera into the image files. This information is detailed in Table II. A method has been developed to compare the results with the final report table to avoid the repetition of located relative hot regions. Only one is considered if there are several points with the same coordinates within a margin.

Table II. Relative hot region locations

| GPS Latitude/Longitude | $X_h/Y_h/H/W$ |
|---|---|
| 38.703757/-4.119919 | 162/82/25/25 |
| 38.703798/-4.120075 | 558/173/15/15 |
| 38.703813/-4.120077 | 562/205/15/15 |
| 38.703910/-4.120043 | 476/406/16/16 |

PV panels that appears partially are not detected and, therefore, relative hot regions are not considered in these areas. An example of the panel detection is shown at the bottom of Figure 16(d), where several panels are partially included in the image but not detected.

A set of 100 thermographic images of the PV solar plant has been analyzed into the approach to validate the proposed methodology. Figure 17 shows an example of different images of the set.
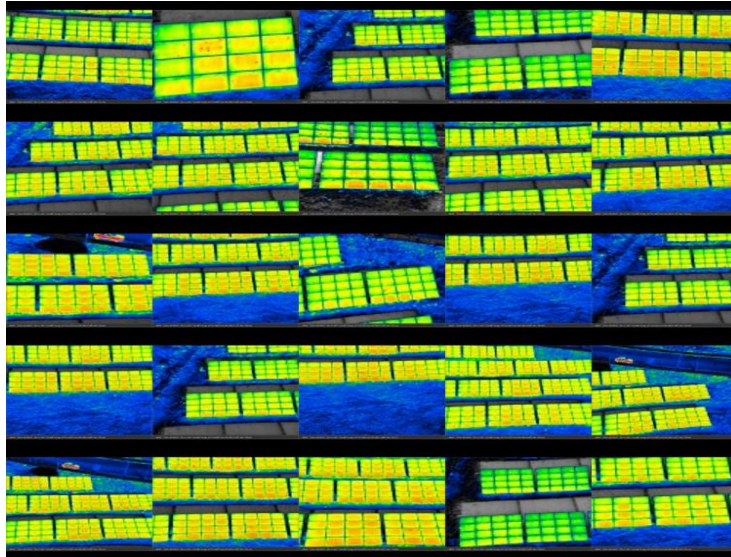
Figure 17. Set of images considered for validation acquired from different angles and perspectives.

The validation will be done according to the detection of PV solar panels and the faults by two confusion matrices. The images are divided into four types of areas, showed in Figure 18, regarding to the concordance between the estimation of the approach and the real case.

Those panels that do not contain any relative hot regions are considered as good panels, otherwise, will be considered as conspicuous panels. Figure 18 shows the possible scenarios for the detection of relative hot regions.
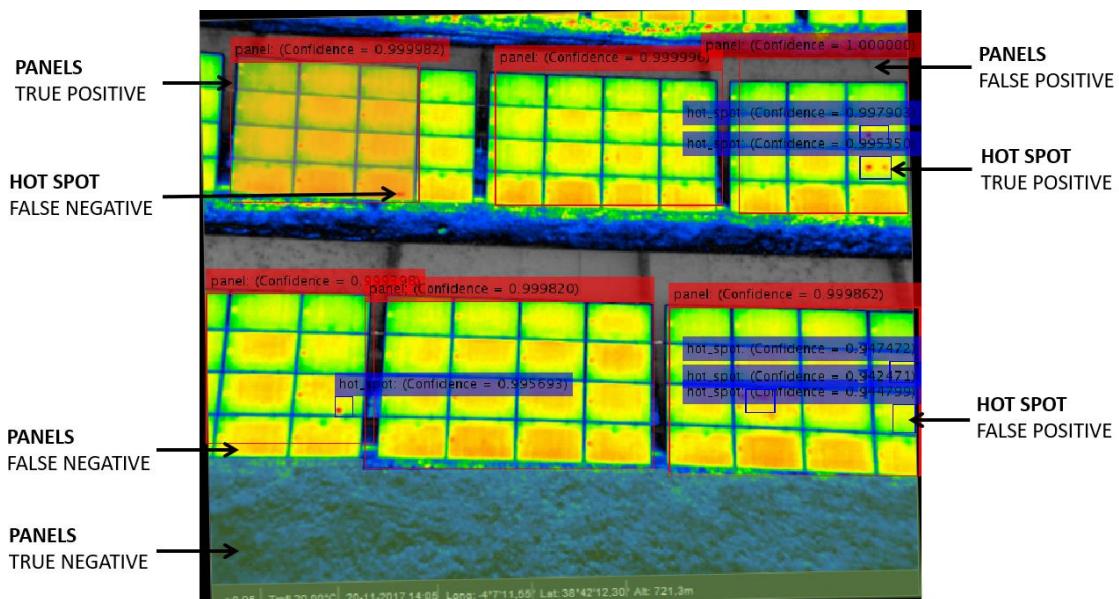


Figure 18. Output of R-CNN panel approach, considering the labels with the confidence percentage obtained by the detector.

The images in Figure 17 are employed to validate the method, and the outcomes are analyzed according to the scenarios given in Figure 18. The statistical characterization of the approach is presented in **¡Error! No se encuentra el origen de la referencia.**. Some standard terms are considered to quantify the performance of both the panel and the relative hot region detectors: accuracy (AC); the true positive rate (TP); false positive rate (FP); true negative rate (TN); the false negative rate (FN), and; precision (P).

Table IIII. Validation metrics for the detection methods

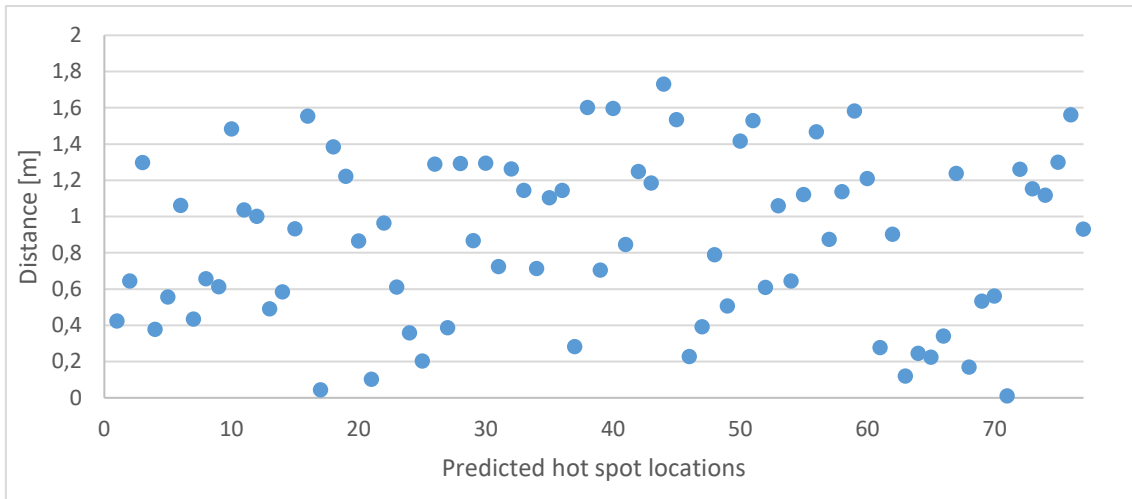| PANEL DETECTION | | Real class | | | Real class | | RELATIVELY HOTTER REGION DETECTION |
|---|---|---|---|---|---|---|---|
| | | Panel | No panel | | Healthy | Damaged | |
| Predicted class | Panel | 40.91% | 2.37% | | 1536 | 9 | Healthy / Predicted class |
| | No Panel | 5.37% | 51.28% | | 7 | 77 | Damaged / Predicted class |
| AC | | 0.9225 | | | 0.9902 | | AC |
| TP | | 0.8840 | | | 0.8953 | | TP |
| FP | | 0.0442 | | | 0.0045 | | FP |
| TN | | 0.9558 | | | 0.9955 | | TN |
| FN | | 0.1160 | | | 0.1047 | | FN |
| P | | 0.9452 | | | 0.9167 | | P |

The accuracy of the panel detector, i.e. the ratio of success in the outcomes, is more than 92.25%. The worst characteristic of the panel detector is the FN, in other words, there is an average of 11% of the panels that cannot be detected in a specific image. These misdetections are due to some panels do not appear completely in the image. However, the complete panels are detected with a higher accuracy. It must be highlighted that the approach has a precision of 94.52%.

Regarding the relative hot region detector, the accuracy is more that 99%. Since the panel detector has a high false negative rate, this error is extended to the relative hot region detector, being the precision more than 91%.

The equipment employed in the inspection are:

- Drone DJI S900
- IR Camera: WIRIS WORKSWELL
- Flight controller: DJI A2
- Gimbal system: Gremsy, T1

The specifications show that the GPS in the flight controller has ±0.5 m vertical error and ±1.5 m horizontal error [77]. According to the gimbal specifications, the zenithal and azimuthal angles can have an error margin of 0.005º [78]. Considering a maximum altitude of 50 m, and a minimum zenithal angle of 30º, the maximum error introduced in the location is estimated to 1.8 m. The validation of the localization method has been done by using a thermal IR camera with a GPS. The validation process consisted in the manual checking of all the relative hot spots locations that were predicted by the proposed algorithm. This process is divided in three steps for each predicted hot spot: first, the location predicted by the algorithm is found using the manual GPS; second, the location of the nearest hotspot is registered, and; third, the distance between both locations is evaluated. The absolute distances obtained are shown in Figure 19.

Figure 19. Absolute distances between the predicted GPS coordinates and the real GPS coordinates of the detected hotspots. Each point indicates the error of the model for each predicted location.

In this case study, an average error of 0.86 m has been achieved and all the errors were below to the estimated threshold of 1.8 m (minimal distance to classify a solar tracker). The solar trackers are longer than this threshold, and there is also space between them, therefore, the localization is done correctly. Due to the positioning error, this methodology does not guarantee the correct localization of the faulty PV panel, but the corresponding solar tracker is identified. This error is not a significative drawback, since all the detected anomalies must be checked manually before doing any repairment or replacement. Therefore, the coordinates of the affected PV trackers are enough to help the operators search for faulty panels.

## 6. Conclusions

This paper has presented a methodology for the detection of faults in photovoltaic solar panels employing data from a thermography camera embedded in an unmanned aerial vehicle. An autonomous and automatic panel and relative hot region detection approach has been designed based on region-based convolutional neural networks. Inspections by unmanned aerial vehicles based usually provide heterogenous images due to the altitude, the orientation, the recording angle, etc. The approach has been demonstrated to be robust and it is validated. The results show that the methodology is adequate for the automatic detection and localization of solar trackers and relative hot regions with and accuracy more than 99.02% and a precision of 91.67%. The PV set and the relative hot spots are located correctly considering the errors found in the experiments. An average error of 0.86 m has been calculated for the localization of relative hot spots.

## Acknowledgements

# References

1.  Agency, I.R.E. Renewable power generation costs in 2017. January 2018, 2018, p 160.
2.  Muñoz, C.Q.G.; Jiménez, A.A.; Márquez, F.P.G. Wavelet transforms and pattern recognition on ultrasonic guides waves for frozen surface state diagnosis. *Renewable Energy* **2018**, *116*, 42-54.
3.  Faza, A. A probabilistic model for estimating the effects of photovoltaic sources on the power systems reliability. *Reliability Engineering & System Safety* **2018**, *171*, 67-77.
4.  Jiménez, A.A.; Muñoz, C.Q.G.; Márquez, F.P.G. Dirt and mud detection and diagnosis on a wind turbine blade employing guided waves and supervised learning classifiers. *Reliability Engineering & System Safety* **2019**, *184*, 2-12.
5.  Martin, A. Soitu.Es http://www.soitu.es/soitu/2009/06/02/medioambiente/1243938326_268516.html (06/13),
6.  Limited, K.S.P.D.C. 2000 mw solar park. http://kspdcl.in/slrprk.htm (March, 5),
7.  Marquez, F.G. An approach to remote condition monitoring systems management. *IET International Conference on Railway Condition Monitoring* **2006**, pp. 156-160.
8.  Pedregal, D.J.; García, F.P.; Roberts, C. An algorithmic approach for maintenance management based on advanced state space systems and harmonic regressions. *Annals of Operations Research* **2009**, *166*, 109-124.
9.  Hatti, M. Operation and maintenance methods in solar power plants. In *Use, operation and maintenance of renewable energy systems*, Springer: 2014; pp 61-93.
10. Andy Warkel, N. Pv o&m cost model and cost reduction. *2017 Photovoltaic Module Reliability Workshop* **2017**, 27.
11. Denio, H. In *Aerial solar thermography and condition monitoring of photovoltaic systems*, Photovoltaic Specialists Conference (PVSC), 2012 38th IEEE, 2012; IEEE: pp 000613-000618.
12. Han, C.; Lee, H. A field-applicable health monitoring method for photovoltaic system. *Reliability Engineering & System Safety* **2019**, *184*, 219-227.
13. Márquez, F.P.G.; Pedregal, D.J.; Roberts, C. New methods for the condition monitoring of level crossings. *International Journal of Systems Science* **2015**, *46*, 878-884.
14. Pliego Marugán, A.; García Márquez, F.P.; Lev, B. Optimal decision-making via binary decision diagrams for investments under a risky environment. *International Journal of Production Research* **2017**, 1-16.
15. Pliego Marugán, A.; García Márquez, F.P.; Pinar Pérez, J.M. Optimal maintenance management of offshore wind farms. *Energies* **2016**, *9*, 46.
16. Márquez, F.P.G.; Pérez, J.M.P.; Marugán, A.P.; Papaelias, M. Identification of critical components of wind turbines using fta over the time. *Renewable Energy* **2016**, *87*, 869-883.
17. García Márquez, F.P.; Pliego Marugán, A.; Pinar Pérez, J.M.; Hillmansen, S.; Papaelias, M. Optimal dynamic analysis of electrical/electronic components in wind turbines. *Energies* **2017**, *10*, 1111.
18. Gupta, S.G.; Ghonge, M.M.; Jawandhiya, P. Review of unmanned aircraft system (uas). *International journal of advanced research in computer engineering & technology (IJARCET)* **2013**, *2*, pp: 1646-1658.
19. Colomina, I.; Molina, P. Unmanned aerial systems for photogrammetry and remote sensing: A review. *ISPRS Journal of Photogrammetry and Remote Sensing* **2014**, *92*, 79-97.
20. Ebner, R.; Kubicek, B.; Ujvari, G. In *Non-destructive techniques for quality control of pv modules: Infrared thermography, electro-and photoluminescence imaging*, Industrial Electronics Society, IECON 2013-39th Annual Conference of the IEEE, 2013; IEEE: pp 8104-8109.
21. Tsanakas, J.; Botsaris, P. Passive and active thermographic assessment as a tool for condition-based performance monitoring of photovoltaic modules. *Journal of Solar Energy Engineering* **2011**, *133*, 021012.

22. Measure. Drones in solar. Benefits, use cases, and best practices for drones in the solar industry today. https://www.measure.com (12/09/2019),

23. Buerhop, C.; Schlegel, D.; Niess, M.; Vodermayer, C.; Weißmann, R.; Brabec, C. Reliability of ir-imaging of pv-plants under operating conditions. *Solar Energy Materials and Solar Cells* **2012**, *107*, 154-164.

24. Persson, D.; Andersson, J. Real-time image processing on handheld devices and uav. Linköping University: 2016; Vol. 1.

25. Márquez, F.P.G.; Ramírez, I.S. Condition monitoring system for solar power plants with radiometric and thermographic sensors embedded in unmanned aerial vehicles. *Measurement* **2019**, *139*, 152-162.

26. Acciani, G.; Simione, G.; Vergura, S. In *Thermographic analysis of photovoltaic panels*, International Conference on Renewable Energies and Power Quality (ICREPQ'10), Granada, Spain, March, 2010; pp 23-25.

27. Maldague, X. *Theory and practice of infrared technology for nondestructive testing.* . 2001; Vol. 1. ISBN: 978-0-47118-190-3.

28. Muñoz, J.; Lorenzo, E.; Martínez‐Moreno, F.; Marroyo, L.; García, M. An investigation into hot‐spots in two large grid‐connected pv plants. *Progress in Photovoltaics: Research and applications* **2008**, *16*, 693-701.

29. Aghaei, M.; Quater, P.B.; Grimaccia, F.; Leva, S.; Mussetta, M. In *Unmanned aerial vehicles in photovoltaic systems monitoring applications*, 29th European Photovoltaic Solar Energy Conference and Exhibition, 2014; pp 2734-2739.

30. Kim, D.; Youn, J.; Kim, C. Automatic fault recognition of photovoltaic modules based on statistical analysis of uav thermography. *ISPRS-International Archives of the Photogrammetry, Remote Sensing and Spatial Information Sciences* **2017**, 179-182.

31. Kim, D.; Youn, J.; Kim, C. Automatic photovoltaic panel area extraction from uav thermal infrared images. *Journal of the Korean Society of Surveying, Geodesy, Photogrammetry and Cartography* **2016**, *34*, 559-568.

32. Tsanakas, J.A.; Ha, L.D.; Al Shakarchi, F. Advanced inspection of photovoltaic installations by aerial triangulation and terrestrial georeferencing of thermal/visual imagery. *Renewable Energy* **2017**, *102*, 224-233.

33. Marugán, A.P.; Márquez, F.P.G.; Perez, J.M.P.; Ruiz-Hernández, D. A survey of artificial neural network in wind energy systems. *Applied Energy* **2018**, *228*, 1822-1836.

34. Molenbroek, E.; Waddington, D.; Emery, K. In *Hot spot susceptibility and testing of pv modules*, Photovoltaic Specialists Conference, 1991., Conference Record of the Twenty Second IEEE, 1991; IEEE: pp 547-552.

35. Girshick, R.; Donahue, J.; Darrell, T.; Malik, J. In *Rich feature hierarchies for accurate object detection and semantic segmentation*, Proceedings of the IEEE conference on computer vision and pattern recognition, 2014; pp 580-587.

36. Redmon, J.; Divvala, S.; Girshick, R.; Farhadi, A. In *You only look once: Unified, real-time object detection*, Proceedings of the IEEE conference on computer vision and pattern recognition, 2016; pp 779-788.

37. Yue-Hei Ng, J.; Hausknecht, M.; Vijayanarasimhan, S.; Vinyals, O.; Monga, R.; Toderici, G. In *Beyond short snippets: Deep networks for video classification*, Proceedings of the IEEE conference on computer vision and pattern recognition, 2015; pp 4694-4702.

38. Qian, R.; Liu, Q.; Yue, Y.; Coenen, F.; Zhang, B. In *Road surface traffic sign detection with hybrid region proposal and fast r-cnn*, Natural Computation, Fuzzy Systems and Knowledge Discovery (ICNC-FSKD), 2016 12th International Conference on, 2016; IEEE: pp 555-559.

39. Kim, H.; Lee, Y.; Yim, B.; Park, E.; Kim, H. In *On-road object detection using deep neural network*, Consumer Electronics-Asia (ICCE-Asia), IEEE International Conference on, 2016; IEEE: pp 1-4.

40. ARMENTA, D.M.R. Diagnosis of breast cancer through the processing of thermographic images and neural networks. **2017**.

41.   Farfade, S.S.; Saberian, M.J.; Li, L.-J. In *Multi-view face detection using deep convolutional neural networks*, Proceedings of the 5th ACM on International Conference on Multimedia Retrieval, 2015; ACM: pp 643-650.

42.   Hernandez, C.; Bharatheesha, M.; Ko, W.; Gaiser, H.; Tan, J.; van Deurzen, K.; de Vries, M.; Van Mil, B.; van Egmond, J.; Burger, R. In *Team delft's robot winner of the amazon picking challenge 2016*, Robot World Cup, 2016; Springer: pp 613-624.

43.   Wang, J.; Garratt, M.; Lambert, A.; Wang, J.J.; Han, S.; Sinclair, D. Integration of gps/ins/vision sensors to navigate unmanned aerial vehicles. *The International Archives of the Photogrammetry, Remote Sensing and Spatial Information Sciences* **2008**, *37*, 963-970.

44.   Ancuta, F.; Cepisca, C. In *Fault analysis possibilities for pv panels*, Energetics (IYCE), Proceedings of the 2011 3rd International Youth Conference on, 2011; IEEE: pp 1-5.

45.   Hu, Y.; Cao, W.; Ma, J.; Finney, S.J.; Li, D. Identifying pv module mismatch faults by a thermography-based temperature distribution analysis. *IEEE Transactions on Device and Materials Reliability* **2014**, *14*, 951-960.

46.   Márquez, F.P.G.; Pedregal, D.J. Applied rcm 2 algorithms based on statistical methods. *International Journal of Automation and Computing* **2007**, *4*, 109-116.

47.   García Márquez, F.P.; García‑Pardo, I.P. Principal component analysis applied to filtered signals for maintenance management. *Quality and Reliability Engineering International* **2010**, *26*, 523-527.

48.   Márquez, F.P.G.; Muñoz, J.M.C. A pattern recognition and data analysis method for maintenance management. *International Journal of Systems Science* **2012**, *43*, 1014-1028.

49.   Muñoz, C.Q.G.; Márquez, F.P.G.; Tomás, J.M.S. Ice detection using thermal infrared radiometry on wind turbine blades. *Measurement* **2016**, *93*, 157-163.

50.   Köntges, M.; Kurtz, S.; Packard, C.; Jahn, U.; Berger, K.A.; Kato, K.; Friesen, T.; Liu, H.; Van Iseghem, M.; Wohlgemuth, J. Review of failures of photovoltaic modules. **2014**.

51.   Pingel, S.; Frank, O.; Winkler, M.; Daryan, S.; Geipel, T.; Hoehne, H.; Berghold, J. In *Potential induced degradation of solar cells and panels*, 2010 35th IEEE Photovoltaic Specialists Conference, 2010; IEEE: pp 002817-002822.

52.   Flir. Specifications of flir vue pro. https://www.flir.com/support/products/vue-pro#Specifications (12/10/2018),

53.   Dunlop, J. Why you should know what focal length means. https://expertphotography.com/understand-focal-length-4-easy-steps/ (06/18/2018),

54.   Usamentiaga, R.; Venegas, P.; Guerediaga, J.; Vega, L.; Molleda, J.; Bulnes, F.G. *Infrared thermography for temperature measurement and non-destructive testing*. 2014; Vol. 14, p 12305-12348.

55.   Krizhevsky, A.; Sutskever, I.; Hinton, G.E. In *Imagenet classification with deep convolutional neural networks*, Advances in neural information processing systems, 2012; pp 1097-1105.

56.   Yadav, J.S.; Yadav, M.; Jain, A. Artificial neural network. *International Journal of Scientific Research and Education* **2014**, *1*, 108-117.

57.   Peng, M.; Wang, C.; Chen, T.; Liu, G. Nirfacenet: A convolutional neural network for near-infrared face identification. *Information* **2016**, *7*, 61.

58.   Khoshdeli, M.; Cong, R.; Parvin, B. In *Detection of nuclei in h&e stained sections using convolutional neural networks*, Biomedical & Health Informatics (BHI), 2017 IEEE EMBS International Conference on, 2017; IEEE: pp 105-108.

59.   Hariharan, B.; Arbeláez, P.; Girshick, R.; Malik, J. In *Simultaneous detection and segmentation*, European Conference on Computer Vision, 2014; Springer: pp 297-312.

60.   Gkioxari, G.; Hariharan, B.; Girshick, R.; Malik, J. R-cnns for pose estimation and action detection. *arXiv preprint arXiv:1406.5212* **2014**.

61.   Karpathy, A. Convolutional neural networks (cnns / convnets). http://cs231n.github.io/convolutional-networks/ (20/06),

62.   Kuo, C.-C.J. Understanding convolutional neural networks with a mathematical model. *Journal of Visual Communication and Image Representation* **2016**, *41*, 406-413.

63. Nair, V.; Hinton, G.E. In *Rectified linear units improve restricted boltzmann machines*, Proceedings of the 27th international conference on machine learning (ICML-10), 2010; pp 807-814.

64. Jiménez, A.A.; Márquez, F.P.G.; Moraleda, V.B.; Muñoz, C.Q.G. Linear and nonlinear features and machine learning for wind turbine blade ice detection and diagnosis. *Renewable Energy* **2019**, *132*, 1034-1048.

65. Hinton, G.E.; Salakhutdinov, R.R. In *Replicated softmax: An undirected topic model*, Advances in neural information processing systems, 2009; pp 1607-1614.

66. Tang, Y. Deep learning using linear support vector machines. *arXiv preprint arXiv:1306.0239* **2013**.

67. Liu, W.; Wen, Y.; Yu, Z.; Yang, M. In *Large-margin softmax loss for convolutional neural networks*, ICML, 2016; p 7.

68. Girshick, R. In *Fast r-cnn*, Proceedings of the IEEE international conference on computer vision, 2015; pp 1440-1448.

69. Pascanu, R.; Mikolov, T.; Bengio, Y. In *On the difficulty of training recurrent neural networks*, International Conference on Machine Learning, 2013; pp 1310-1318.

70. Hoffer, E.; Hubara, I.; Soudry, D. In *Train longer, generalize better: Closing the generalization gap in large batch training of neural networks*, Advances in Neural Information Processing Systems, 2017; pp 1731-1741.

71. Bayar, B.; Stamm, M.C. Design principles of convolutional neural networks for multimedia forensics. *Electronic Imaging* **2017**, *2017*, 77-86.

72. MathWorks. Network layer for deep learning. http://es.mathworks.com/help/deeplearning/ref/nnet.cnn.layer.layer.html?searchHighlight=layer&s_tid=doc_srchtitle (October, 29),

73. Santos, L.A. Artificial inteligence. GitBook, Ed. GitBook: https://leonardoaraujosantos.gitbooks.io/artificial-inteligence.

74. Ren, S.; He, K.; Girshick, R.; Sun, J. In *Faster r-cnn: Towards real-time object detection with region proposal networks*, Advances in neural information processing systems, 2015; pp 91-99.

75. Vijayarani, S.; Vinupriya, M. Performance analysis of canny and sobel edge detection algorithms in image mining. *International Journal of Innovative Research in Computer and Communication Engineering* **2013**, *1*, 1760-1767.

76. Maroto, A.; Boqué, R.; Riu, J.; Rius, F.X. Incertidumbre y precisión. In *Tecnicas de laboratorio-barcelona-*, 2001; pp 834-839.

77. DJI. A2 fligth controller. https://www.dji.com/uk/a2 (18-10-2019),

78. Gremsy. Gremsy t1, specifications. . https://gremsy.com/gremsy-t1/ (19-10-2019),